

Relativistic MHD with Adaptive Mesh Refinement

Matthew Anderson¹, Eric W. Hirschmann², Steven L. Liebling³,
David Neilsen²

¹ Department of Physics and Astronomy, Louisiana State University, Baton Rouge, LA 70803-4001, USA

² Department of Physics and Astronomy, Brigham Young University, Provo, UT 84602, USA

³ Department of Physics, Long Island University – C.W. Post Campus, Brookville, NY 11548, USA

Abstract. This paper presents a new computer code to solve the general relativistic magnetohydrodynamics (GRMHD) equations using distributed parallel adaptive mesh refinement (AMR). The fluid equations are solved using a finite difference Convex ENO method (CENO) in $3 + 1$ dimensions, and the AMR is Berger-Oliger. Hyperbolic divergence cleaning is used to control the $\nabla \cdot \mathbf{B} = 0$ constraint. We present results from three flat space tests, and examine the accretion of a fluid onto a Schwarzschild black hole, reproducing the Michel solution. The AMR simulations substantially improve performance while reproducing the resolution equivalent unigrid simulation results. Finally, we discuss strong scaling results for parallel unigrid and AMR runs.

1. Introduction

The interaction of gravitational and electromagnetic fields together with rotation is believed to power the central engines of many astrophysical phenomena including relativistic jets in active galactic nuclei (AGN), other forms of black hole accretion, gamma-ray bursts (GRB), and core collapse supernovae. In addition, interactions between strong gravitational and electromagnetic fields are believed to result in the transport of angular momentum in accretion disks via the magnetorotational instability (MRI) and in the extraction of black hole energy via the Blandford-Znajek mechanism.

The expected ubiquity of magnetic fields in the vicinity of strongly gravitating compact objects has spurred increased theoretical efforts to understand these astrophysical systems. The difficulties, however, are formidable as the physical laws describing these phenomena are nonlinear, evolutionary, and, in general, without simplifying symmetries. As a consequence, numerical simulation of these systems becomes crucial for better understanding them. Even then, there are likely considerable aspects of the physics that remain out of reach of current computational resources. For instance, it is not unrealistic to imagine that dissipative and radiative aspects of these problems will be important for accurately modeling certain types of phenomena. However, with the hope of capturing some of the relevant physics, a number of groups have begun developing methods and codes for evolving some of the relativistic components of these complicated scenarios.

In this large and growing body of work, a significant effort is directed at special relativistic magnetohydrodynamics (RMHD). However, with increasing interest in the interaction of gravitational and electromagnetic fields, one must also couple the equations of relativistic MHD to general relativity either through a curved space background or the

dynamical field equations themselves. The earliest attack on this general problem was Wilson's pioneering work evolving a rotating, axisymmetric star with a poloidal magnetic field [1]. Subsequently, little numerical work was done until very recently with several groups developing codes for evolving the general relativistic MHD (GRMHD) equations on fixed backgrounds [2, 3, 4, 5, 6, 7, 8] and in dynamical spacetimes [9, 10].

One of the difficulties alluded to above in the numerical simulation of these sorts of systems is that one must solve the GRMHD equations over a large range of time and length scales. The computational requirements necessary to adequately resolve multiscale phenomena using only a single resolution mesh are often too high for available resources. This is particularly true when the full, dynamical GRMHD equations are being considered. Adaptive mesh refinement (AMR) therefore becomes crucial in order to reduce the computational requirements necessary for modeling such systems.

There are currently MHD codes in use which incorporate AMR, but most are focused on the nonrelativistic problem [11, 12, 13]. Notable among these are the work of Balsara which extended a version of constrained transport to AMR. For relativistic MHD, only the work by Anninos *et al* [8] incorporates adaptive mesh refinement. Theirs is a finite volume approach with divergence cleaning.

This paper describes our algorithm for solving the GRMHD equations with AMR. Building on the work presented in [14], where the RMHD equations were solved on overlapping grids, some key elements of our algorithm are: (1) The Convex Essentially Non-Oscillatory (CENO) method for the MHD equations, (2) Hyperbolic divergence cleaning for controlling the solenoidal constraint, (3) Berger-Oliger AMR, (4) Weighted Essentially Non-Oscillatory (WENO) interpolation for communications from coarse to fine grids, and (5) discretization in time via method of lines.

The CENO scheme is robust, and has three advantages for our code. First, the method does not require the spectral decomposition of the Jacobian matrix, making it relatively efficient. Central and central-upwind schemes are known to give results nearly identical to those of more complicated methods for many problems [15, 16]. With the added capability of AMR, we find that we are able to efficiently resolve very fine solution features. A second advantage of CENO for our purposes is that it is a finite difference, or vertex centered, method. As we will solve the Einstein equations with finite differences, using a finite difference fluid scheme simplifies coupling the two sets of equations with AMR. The simplification arises because fluid and geometric variables are always defined at the same point as grids are refined. Finite volume and finite difference grids become staggered with respect to each other as they are refined. While we find this simplification advantageous in our present work, we note that our AMR code HAD can combine finite difference and finite volume schemes [17]. A third advantage is that ENO schemes are easily extended to higher order accuracy. Our CENO scheme can reconstruct fluid variables to both first and second order, resulting in second and third order evolution schemes, respectively.

We choose hyperbolic divergence cleaning [18] to limit growth in the solenoidal constraint on the magnetic field, $\nabla \cdot \mathbf{B} = 0$. Hyperbolic divergence cleaning is simple to implement. A single hyperbolic field is added to the system and coupled to the evolution equations for \mathbf{B} . Divergence cleaning gave good results in earlier tests [14] and allows us to freely choose prolongation methods for AMR. While $\nabla \cdot \mathbf{B} = 0$ is not satisfied to machine precision for any particular discrete divergence operator, we find that $\|\nabla \cdot \mathbf{B}\|$ does converge to zero, and, in the tests presented here, $\|\nabla \cdot \mathbf{B}\|$ is roughly the same order of magnitude as the expected truncation error.

Mesh refinement is necessary for obtaining accurate numerical solutions for three dimensional systems in general relativity, and AMR is essential for complicated problems

where the refinement regions can not be guessed *a priori*. We use the HAD infrastructure to provide Berger-Oliger style AMR [19]. HAD has a modular design allowing one to easily implement many different sets of evolution equations, and different modules can be combined, for example, to solve both the Einstein and MHD equation simultaneously. HAD supports higher order differencing schemes, and our implementation of the MHD equations is fully third order accurate [20]. Refinement regions can be specified in a variety of ways. HAD provides a shadow hierarchy for specifying refinement criteria using truncation error estimates, or the user may specify problem specific criteria, such as refining on gradients or other solution features. HAD supports different interpolation schemes (we choose WENO interpolation for this work) and supports both finite volume and finite difference equations or combinations of both. Finally, as discussed below, HAD scales well in strong scaling tests in both unigrid and AMR tests.

Finally, we discretize the continuum equations first in space (creating a semi-discrete system) and then discretize in time using the method of lines. This gives us considerable flexibility in choosing discretization schemes appropriate for very different types of equations. For example, the MHD equations are solved here with high-resolution shock-capturing methods, while we might solve the Einstein equations using methods that preserve a discrete energy norm. Using the method of lines, we can easily and consistently combine these two sets of semi-discrete equations in a uniform time integration. Time integrators can be independently chosen for their desired properties or order of integration. For example, we choose for this work a third-order Runge–Kutta scheme that preserves the TVD condition [21].

The remaining sections of this paper give further details to the algorithm sketched above and present code tests in both flat space and on a Schwarzschild black hole background. We first present the GRMHD equations used in this work.

2. The MHD equations in general relativity

A number of derivations of the GRMHD equations have appeared in the literature, e.g., [22, 23, 24, 25, 4, 3, 14], and thus we simply present the equations to be solved here. The numerical methods that we use are very similar to those we have used in our previous MHD work using overlapping grids. Thus our presentation here is short, and the reader may refer to that work for more detail [14].

The spacetime metric is written in terms of the conventional ADM 3+1 variables, namely

$$ds^2 = -\alpha^2 dt^2 + h_{ij}(dx^i + \beta^i dt)(dx^j + \beta^j dt), \quad (1)$$

where α is the lapse, β^i is the shift, and h_{ij} is the 3-metric on the spacelike hypersurfaces. Units are chosen such that $c = 1$ and $G = 1$. We denote the extrinsic curvature as K_{ab} and the Christoffel coefficients with respect to the 3-metric as ${}^3\Gamma_{ab}^i$. As our focus in this paper is fixed background geometries, we will omit here a discussion of our approach to evolving the Einstein equations and only present the relevant matter equations. Future papers will address dynamical spacetimes.

The equations for MHD on a curved background, as in flat spacetime, can be written, for the most part, in balance law form, namely

$$\partial_t \mathbf{u} + \partial_k \mathbf{f}^k(\mathbf{u}) = \mathbf{s}(\mathbf{u}). \quad (2)$$

where \mathbf{u} is a state vector, \mathbf{f}^k are flux functions, and \mathbf{s} are source terms. For the current case, these are

$$\partial_t \left(\sqrt{h} D \right) + \partial_i \left[\sqrt{-g} D \left(v^i - \frac{\beta^i}{\alpha} \right) \right] = 0, \quad (3)$$

$$\begin{aligned} \partial_t \left(\sqrt{h} S_b \right) + \partial_i \left[\sqrt{-g} \left(S_b \left(v^i - \frac{\beta^i}{\alpha} \right) + P h^i_b - \frac{1}{W^2} \left(B^i B_b - \frac{1}{2} h^i_b B^j B_j \right) \right. \right. \\ \left. \left. - \frac{1}{2} B^j v_j \left(B^i v_b - \frac{1}{2} h^i_b B^j v_j \right) \right) \right] \\ = \sqrt{-g} \left[{}^3\Gamma_{ab}^i (\perp T)^a_i + \frac{1}{\alpha} S_a \partial_b \beta^a - \frac{1}{\alpha} \partial_b \alpha E \right], \end{aligned} \quad (4)$$

$$\partial_t \left(\sqrt{h} \tau \right) + \partial_i \left[\sqrt{-g} \left(S^i - \frac{\beta^i}{\alpha} \tau - v^i D \right) \right] = \sqrt{-g} \left[(\perp T)^{ab} K_{ab} - \frac{1}{\alpha} S^a \partial_a \alpha \right], \quad (5)$$

$$\partial_t \left(\sqrt{h} B^b \right) + \partial_i \left[\sqrt{-g} \left(B^b \left(v^i - \frac{\beta^i}{\alpha} \right) - B^i \left(v^b - \frac{\beta^b}{\alpha} \right) \right) \right] = 0, \quad (6)$$

$$\frac{1}{\sqrt{h}} \partial_i \left(\sqrt{h} B^i \right) = 0, \quad (7)$$

where the quantity $(\perp T)^i_b$ is the spatial projection of the stress tensor given in terms of the matter fields by

$$\begin{aligned} (\perp T)^i_b = v^i S_b + P \cdot h^i_b - \frac{1}{W^2} \left[B^i B_b - \frac{1}{2} h^i_b \cdot B^2 \right] \\ - (B^j v_j) \left[B^i v_b - \frac{1}{2} h^i_b \cdot (B^j v_j) \right]. \end{aligned} \quad (8)$$

In the above, we work from a set of “primitive” variables $\mathbf{w} = (\rho_0, v^i, P, B^j)^T$ consisting of the energy density, ρ_0 , the components of the coordinate velocity of the fluid, v^i , the fluid pressure, P , and the magnetic field in the fluid frame, B^j . From these, we define a set of conservative variables, $\mathbf{u} = (D, S_b, \tau, B^j)^T$ where the relativistic density D , momentum S_b , and energy $E = \tau + D$ are given in terms of the primitive variables by

$$D = W \rho_0, \quad (9)$$

$$S_i = [h_e W^2 + B^2] v_i - (B^j v_j) B_i, \quad (10)$$

$$\tau = h_e W^2 + B^2 - P - \frac{1}{2} \left[(B^j v_j)^2 + \frac{B^2}{W^2} \right] - W \rho_0, \quad (11)$$

and B^j remains unchanged. We have also defined $B^2 = B_i B^i$, the fluid enthalpy $h_e = \rho_0(1 + \epsilon) + P$ with ϵ the fluid’s internal energy, and the Lorentz factor $W = (1 - v_i v^i)^{-1/2}$. Note that spatial indices are lowered and raised by the 3-metric h_{ij} and its inverse. Finally, to close the system, we assume a Γ -law equation of state

$$P = (\Gamma - 1) \rho_0 \epsilon, \quad (12)$$

where Γ is the usual adiabatic index. Note that while Eqns. (3)–(6) are indeed in balance law form, Eq. (7) is not. This last equation, of course, is the solenoidal constraint and must be dealt with separately.

One of the benefits of our chosen numerical scheme is that it does not require the full spectral decomposition of the system of evolution equations. However, we do find it useful to have some information about the possible speeds of some of the waves in our system. This information comes by solving for the eigenvalues of the Jacobian matrix, \mathcal{J}^k , associated with the flux, $\mathbf{f}^k(\mathbf{u})$, in the k direction where

$$\mathcal{J}^k = \frac{\partial \mathbf{f}^k(\mathbf{u})}{\partial \mathbf{u}}. \quad (13)$$

On doing this for our system for the k direction, say, one gets the general relativistic generalization [7] of the seven wave speeds of flat space MHD [26, 27, 28, 29]. These include the entropy wave and two Alfvén waves,

$$\text{ent} \lambda^k = \alpha v^k - \beta^k \quad (14)$$

$$\text{A} \lambda_{\pm}^k = \alpha v^k - \beta^k - \frac{B^k}{h_e W^2 + B^2} \left[B^j v_j \pm \left(h_e (B^j v_j)^2 + \frac{B^2}{W^2} \right)^{1/2} \right] \quad (15)$$

and the four (“fast” and “slow”) magnetosonic waves, $^{\text{f,s}} \lambda_{\pm}^k$, that are the zeros of the fourth order polynomial

$$\begin{aligned} 0 = & h_e W^4 (1 - c_s^2) (\alpha v^k - \beta^k - \lambda^k)^4 \\ & + \left[(\beta^k + \lambda^k)^2 - \alpha^2 h^{kk} \right] \cdot \left[(\alpha v^k - \beta^k - \lambda^k)^2 (h_e W^2 c_s^2 + B^2 + W^2 (B^j v_j)^2) \right. \\ & \left. - c_s^2 \left(W (B^j v_j) (\alpha v^k - \beta^k - \lambda^k) + \alpha \frac{B^k}{W} \right)^2 \right] \quad (16) \end{aligned}$$

where c_s is the local sound speed and is given by

$$h_e c_s^2 = \rho_0 \frac{\partial P}{\partial \rho_0} + \frac{P}{\rho_0} \frac{\partial P}{\partial \epsilon}. \quad (17)$$

We solve (16) numerically using the DRTEQ4 routine from the publicly available CERN Program Library. The roots from DRTEQ4 are then refined using a Newton-Raphson solver.

Finally, we note that the MHD equations are written in terms of both the conservative and primitive variables. The transformation from conservative variables to primitive variables is transcendental, requiring the solution of a single transcendental, nonlinear equation, and is outlined in [14].

3. Numerical approach

This section briefly summarizes the numerical scheme we use to solve the relativistic MHD equations. The fluid equations are solved with the Convex Essentially Non-Oscillatory (CENO) scheme. CENO is based on a finite difference discretization, which simplifies the coupling to the Einstein equations with AMR. Hyperbolic divergence cleaning controls growth of error in the solenoidal constraint, and gives some flexibility in choosing other components of the numerical algorithm with AMR.

3.1. CENO

The CENO scheme was developed by Liu and Osher [30] to efficiently solve equations in balance law form

$$\partial_t \mathbf{u} + \partial_k \mathbf{f}^k(\mathbf{u}) = \mathbf{s}(\mathbf{u}), \quad (18)$$

where \mathbf{u} is a state vector, \mathbf{f}^k are flux functions, and \mathbf{s} source terms. We use the modification of CENO for relativistic fluids of Del Zanna and Bucciantini [31]. Equation (18) is solved using the method of lines. The semi-discrete form in one dimension is

$$\frac{d\mathbf{u}_i}{dt} = - \frac{\hat{\mathbf{f}}_{i+1/2} - \hat{\mathbf{f}}_{i-1/2}}{\Delta x} + \mathbf{s}(\mathbf{u}_i), \quad (19)$$

where $\hat{\mathbf{f}}$ is a consistent numerical flux. We use both the Lax–Friedrichs flux and the HLL flux for the numerical flux. The Lax–Friedrichs flux is

$$\mathbf{f}_{i+1/2}^{\text{LF}} = \frac{1}{2} \left[\mathbf{f}(\mathbf{u}_{i+1/2}^L) + \mathbf{f}(\mathbf{u}_{i+1/2}^R) - (\mathbf{u}_{i+1/2}^R - \mathbf{u}_{i+1/2}^L) \right], \quad (20)$$

where $\mathbf{u}_{i+1/2}^L$ and $\mathbf{u}_{i+1/2}^R$ are the left and right reconstructed states at $x_{i+1/2}$. The HLL flux [32] is a central-upwind flux that uses the maximum characteristic velocities for both left- and right-moving waves, λ_ℓ and λ_r , respectively,

$$\mathbf{f}^{\text{HLL}} = \frac{\lambda_r^+ \mathbf{f}(\mathbf{u}^\ell) - \lambda_\ell^- \mathbf{f}(\mathbf{u}^r) + \lambda_r^+ \lambda_\ell^- (\mathbf{u}^r - \mathbf{u}^\ell)}{\lambda_r^+ - \lambda_\ell^-}, \quad (21)$$

where

$$\lambda_\ell^- = \min(0, \lambda_\ell) \quad (22)$$

$$\lambda_r^+ = \max(0, \lambda_r). \quad (23)$$

For highly relativistic flows the Lax–Friedrichs flux gives results very similar to the HLL flux; the maximum characteristic velocities approach the speed of light.

The point-valued fluxes $\mathbf{f}_{i+1/2}$ are then converted into consistent numerical fluxes, $\hat{\mathbf{f}}_{i+1/2}$. For a second order scheme, $\hat{\mathbf{f}}_{i+1/2} = \mathbf{f}_{i+1/2}$, while the correction for the third-order scheme is [21]

$$\hat{\mathbf{f}}_{i+1/2} = \left(1 - \frac{1}{24} \mathcal{D}^{(2)}\right) \mathbf{f}_{i+1/2}, \quad (24)$$

where $\mathcal{D}^{(2)}$ is a non-oscillatory second-order difference operator. The operator used in this work is specified in [14].

The accuracy of the overall numerical scheme is determined by the reconstruction of the fluid states $\mathbf{u}_{i+1/2}^L$ and $\mathbf{u}_{i+1/2}^R$ from the solution known at grid points, i.e., the solution at $x_{i-p}, \dots, x_i, \dots, x_{i+q}$ for integer p and q . Linear and quadratic reconstructions discussed below lead to second and third order methods, respectively, for smooth solutions. As is commonly done in relativistic fluid dynamics, we reconstruct the primitive variables rather than the conservative variables. This is because the conservative to primitive variable transformation is transcendental, and computationally rather expensive.

The reconstruction is performed hierarchically, meaning that a reconstruction of order n is calculated from the reconstruction of order $n-1$ using a general algorithm. This allows one to construct schemes of formally very high order. Thus, we first obtain a linear reconstruction, L_i , which is then used to create the second order reconstruction. L_i is defined on the domain $[x_{i-1/2}, x_{i+1/2}]$ as

$$L_i(x) = u_i + u'_i(x - x_i), \quad (25)$$

where u'_i is the limited slope

$$u'_i = \text{minmod}(D_- u_i, D_+ u_i). \quad (26)$$

Here we have defined one-sided and centered difference operators as

$$D_\pm u_i = \pm \frac{u_{i\pm 1} - u_i}{\Delta x}, \quad D_0 u_i = \frac{u_{i+1} - u_{i-1}}{2\Delta x}, \quad (27)$$

and the minmod limiter is

$$\text{minmod}(a_1, a_2, \dots) = \begin{cases} \min\{a_k\} & \text{if all } a_k > 0, \\ \max\{a_k\} & \text{if all } a_k < 0, \\ 0 & \text{otherwise.} \end{cases} \quad (28)$$

The first-order reconstruction, $L_i(x)$, is thus equivalent to the linear TVD reconstruction.

A second order reconstruction proceeds by constructing three candidate quadratic functions, $Q_i^k(x)$, which are then compared to $L_i(x)$. When the solution is smooth, one of the quadratic functions is chosen for the reconstruction. Near discontinuities, however, the linear

reconstruction is retained, thus giving solutions similar to TVD schemes for discontinuous solutions. The three candidate quadratic functions are

$$Q_i^k(x) = u_{i+k} + D_0 u_{i+k}(x - x_{i+k}) + \frac{1}{2} D_+ D_- u_{i+k}(x - x_{i+k})^2, \quad (29)$$

with $k = -1, 0, 1$. Weighted differences with respect to $L_i(x)$ are then calculated

$$d^k(x) = \alpha^k (Q_i^k(x) - L_i(x)). \quad (30)$$

The weights α^k are chosen to bias the reconstruction towards the centered polynomial: $\alpha^0 = 0.7$, and $\alpha^{-1} = \alpha^1 = 1$. When the differences d^k all have the same sign, we choose the $Q_i^k(x)$ for which d^k has the smallest magnitude. When the $d^k(x)$ have differing signs, we revert to the first order reconstruction.

Finally, the semi-discrete equations are integrated with the optimal third-order Runge–Kutta that preserves the TVD condition [21]

$$\begin{aligned} \mathbf{u}^{(1)} &= \mathbf{u}^n + \Delta t L(\mathbf{u}^n), \\ \mathbf{u}^{(2)} &= \frac{3}{4} \mathbf{u}^n + \frac{1}{4} \mathbf{u}^{(1)} + \frac{1}{4} \Delta t L(\mathbf{u}^{(1)}), \\ \mathbf{u}^{n+1} &= \frac{1}{3} \mathbf{u}^n + \frac{2}{3} \mathbf{u}^{(2)} + \frac{2}{3} \Delta t L(\mathbf{u}^{(2)}). \end{aligned} \quad (31)$$

3.2. Hyperbolic Divergence Cleaning

The time evolution of the magnetic field is governed by (6) above. However, \mathbf{B} is also subject to the solenoidal constraint $\nabla \cdot \mathbf{B} = 0$. The continuum evolution equations preserve this constraint, although it may be violated in numerical evolutions. These violations can lead to unphysical numerical solutions [33, 34]. Some differencing schemes for the Maxwell equations and MHD are designed such that a particular discretization of the solenoidal constraint is satisfied to machine precision. These constrained transport methods, naturally, do not give solutions that exactly satisfy the continuum constraint, and the magnitude of the constraint error can be estimated by using an independent discrete divergence operator. Constrained transport methods for classical MHD have been used with AMR [35, 36, 37, 38].

Divergence cleaning methods are an alternative approach to constrained transport, and allow some flexibility in designing the numerical algorithm. Elliptic divergence cleaning methods require the solution of a Poisson equation (either explicitly, or implicitly in Fourier space), and some common implementations have been reviewed for classical MHD by Tóth [39] and Balsara and Kim [40]. Tóth reports favorably on divergence cleaning, while Balsara and Kim argue that constrained transport performs better for a wider class of problems. Hyperbolic divergence cleaning is quite efficient, easy to implement, and usually gives good results [18]. A new field ψ is added to the equations and coupled to the evolution equations for \mathbf{B} . The field ψ acts as a generalized Lagrange multiplier, similar to the λ -system used in solving the Einstein equations [41]. Having some freedom in choosing the equation for ψ , we choose

$$\partial_t B^b + \partial_i (B^b v^i - B^i v^b) + h^{bj} \partial_j \psi = 0, \quad (32)$$

$$\frac{1}{c_h^2} \partial_t \psi + \frac{1}{c_p^2} \psi + \nabla \cdot \mathbf{B} = 0. \quad (33)$$

It can be shown that ψ satisfies the telegraph equation, whose solutions are damped, traveling waves. The parameters c_h and c_p control the speed and damping of the constraint propagation, respectively. We use $c_h = 1$ and $c_p \in [1, 12]$ in the tests examined here. Using larger values of c_h requires smaller Courant factors and did not change results significantly in [14]. In

contrast, the optimal damping factor, c_p , is related to the size of the initial shock discontinuity. Generally, the larger the shock, the larger the value necessary for c_p . Finally, work is underway to develop constraint preserving boundary conditions consistent with hyperbolic divergence cleaning for the MHD equations [42].

3.3. Adaptive Mesh Refinement

AMR provides the ability to add grid refinement where and when needed. This need is determined by some refinement criterion. At any given level of resolution, points which meet this criterion are flagged and a new, finer level is created which includes all such flagged points. Similarly, when no points are flagged, the level is removed. For the tests presented here, the maximum number of levels of refinement was limited to two. In other words, our runs have grids with three different resolutions.

The fine and coarse grids communicate in AMR through prolongation and restriction. Fine grids are created by interpolating the solution from a parent grid (prolongation), and the fine grid solution is communicated to coarser grids through restriction. In prolongation we interpolate the conservative variables onto finer grids using third-order WENO interpolation [43, 14]. This interpolation scheme is designed to work well with discontinuous functions by adjusting the interpolation stencil to the local smoothness of the function. This avoids oscillations near discontinuities, which often cause primitive variable solvers for relativistic fluids to fail. For restriction on vertex centered grids, the fine grid values are copied directly to the coarse grid (direct injection). If a point on a vertex centered coarse grid is also found on two or more finer grids, the restriction operation averages the values on the finer grids for the solution at the coarser grid point.

The distributed AMR infrastructure that we employ is HAD. HAD is a F77 based Berger-Oliger [19] type AMR package presented in [44] using the message passing interface (MPI) for distributed parallelism. HAD has a modular design, allowing one to solve different sets of equations with the same computational infrastructure. Unlike many other publicly available AMR toolkits, including [45, 46, 47, 48, 49], HAD is natively vertex centered. This can be advantageous in numerical relativity, as many difference schemes for the Einstein equations are vertex centered. Support for cell centered grids in HAD is also available. HAD supports subcycling of grids in time for full space-time AMR and can in principle accommodate arbitrary orders of accuracy in both space and time. An example has been shown using third order accurate AMR simulations [20]. The HAD clustering algorithm is Berger-Rigoutsos [50]; the load balancing algorithm is the least loaded scheme [51].

Considerable flexibility is provided in developing a refinement criterion for the HAD infrastructure, and many were explored in conjunction with the numerical tests presented here, such as refining on gradients in the density, pressure or the magnetic field. All criteria resulted in similar adaptive mesh hierarchies for the relativistic rotor and spherical blast wave tests; consequently, those tests center the refinement on the evolving shock front. A shadow hierarchy [52] has recently been added to HAD for truncation error estimation and was used as the refinement criterion in the spherical accretion tests of a fluid falling onto a Schwarzschild black hole.

4. Numerical Results

In this section we examine three relativistic MHD test problems and one accretion test problem using AMR. The MHD test problems are selected because their solutions have very

Balsara blast wave parameters

	ρ_0	P	v^x	v^y	v^z	B^x	B^y	B^z
Left	1.0	1000	0.0	0.0	0.0	10.0	7.0	7.0
Right	1.0	0.1	0.0	0.0	0.0	10.0	0.7	0.7

Table 1. The initial parameters for the Balsara blast wave. The discontinuity is initially placed at $x = 0$ and the system is evolved along the x axis. The adiabatic index is $\Gamma = 5/3$. The exact solution to this problem is given in [53]. The Courant factor used in the numerical solution is 0.2.

sharp features that require high resolutions. The accretion test problem demonstrates the AMR capabilities with a curved space background and an excision region.

The first problem is a one-dimensional blast wave problem introduced by Balsara [11]. We compare the unigrid shocktube results with the exact solution, and then compare unigrid results with the resolution-equivalent AMR results. The second and third problems are three-dimensional extensions of standard two-dimensional tests: a spherical blast wave and a spherical relativistic rotor [28, 10, 14]. We present unigrid and AMR results for these test problems, and discuss the effects of hyperbolic divergence cleaning. The last problem is the accretion of a fluid onto a Schwarzschild black hole. We numerically recover the steady state solution using AMR with a shadow hierarchy as the refinement criterion. Finally, we present scaling results for parallel unigrid and AMR runs. In the tests below we use the discrete L_2 norm

$$\|u\|_2 = \left[\frac{1}{N-1} \sum_i^N (u_i)^2 \right]^{1/2} \quad (34)$$

where u is a discrete function defined at N locations, u_i .

4.1. Riemann problem test

Balsara introduced several test Riemann problems for relativistic MHD [11], and we choose here his third blast wave problem for its very narrow features as a test of our AMR. The initial parameters for this Riemann problem are given in table 1. The exact solution for this problem is given by Giacomazzo and Rezzolla [53], and is plotted in the figures below for comparison.

The blast wave problem is implemented using the three-dimensional HAD infrastructure for AMR and simulated along a coordinate axis. Figure 1 shows the blast wave with a strong initial pressure difference centered at $x = 0$ evolved along the x -axis at several unigrid resolutions. The plots show ρ_0 , v^x , v^y , and B^y at time $t = 0.4$. The unigrid simulations were performed in the x direction on a domain of $[-0.5, 0.5]$ with a Courant factor of 0.2.

A series of two-level AMR simulations of the blast wave test were conducted with refinement centered on the shock propagation. Figure 2 compares a unigrid simulation with a two-level AMR simulation where the resolution of the finest mesh in the AMR hierarchy is the same as that in the unigrid simulation. The AMR capability to reproduce the resolution-equivalent unigrid result depends on how well the refinement region tracks the shock throughout the time history of the evolution. In our tests we observe the AMR blast wave simulations reproducing the resolution-equivalent unigrid result to within 0.1%.

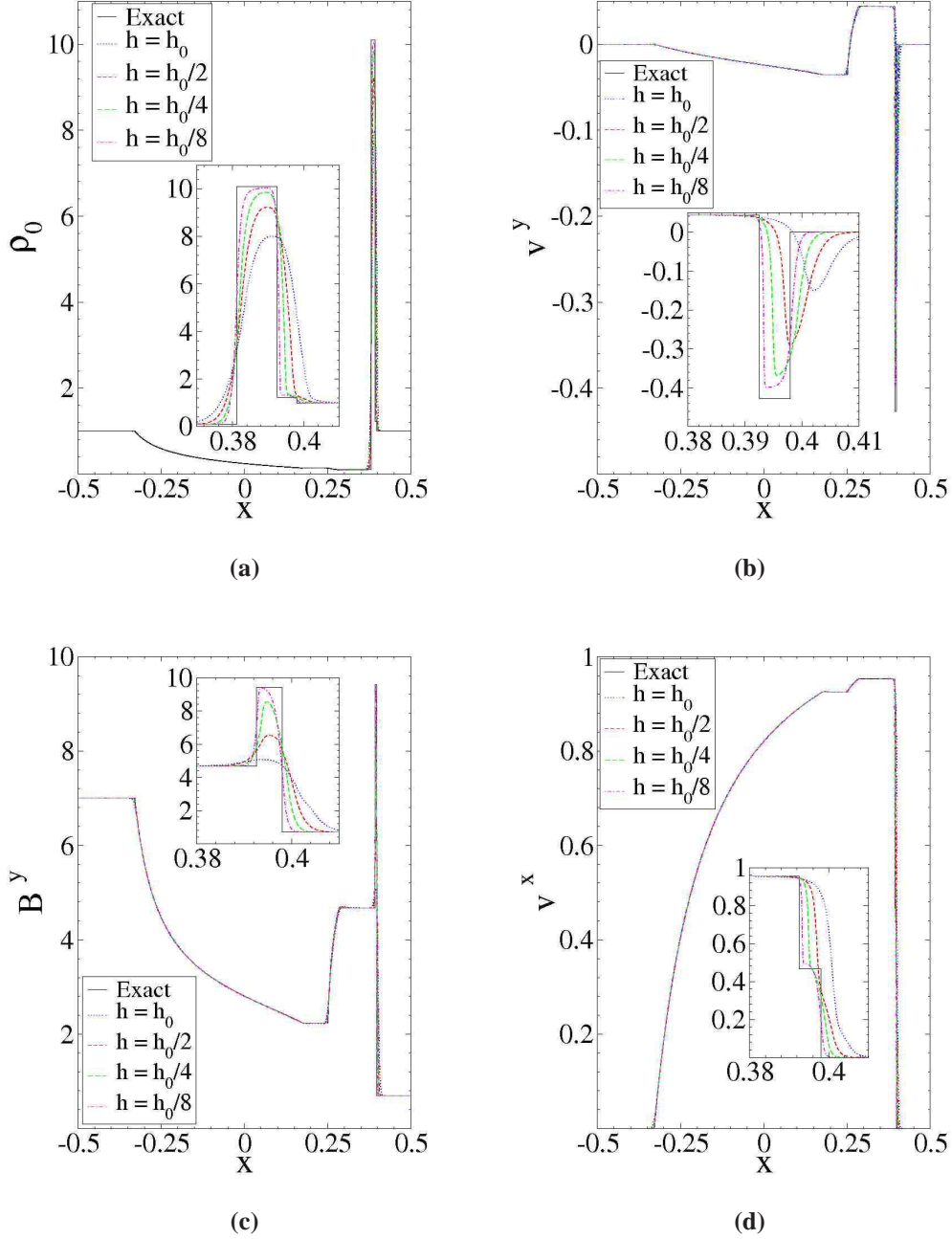


Figure 1. Unigridd simulation results for the relativistic MHD Balsara blast wave test at time 0.4 showing ρ_0 , v^x , v^y , and B^y . The z components of \mathbf{B} and \mathbf{v} are identical to their respective y components. The simulations were performed along the x axis using four resolutions on a domain of $[-0.5, 0.5]$. The base resolution was $h_0 = 6.25 \times 10^{-4}$. The exact solution to this problem is found in [53]. This problem is an excellent candidate for AMR because of the high resolutions required to adequately resolve the different waves.

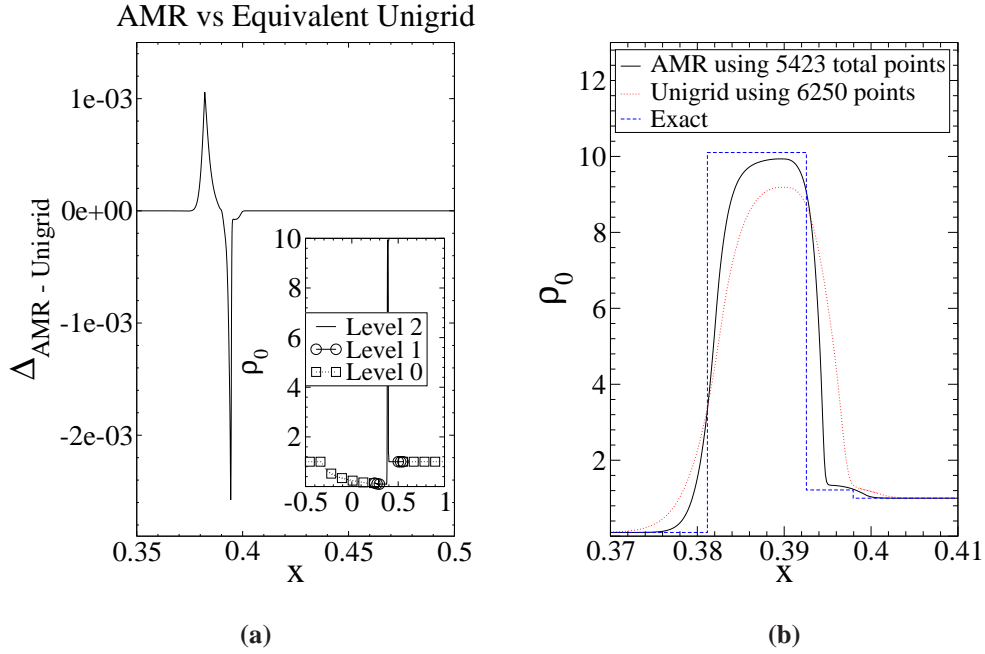


Figure 2. Adaptive mesh refinement results for the Balsara blast wave. Figure 2(a) shows the difference in ρ_0 between the finest mesh in a two-level AMR simulation and the equivalent unigrid simulation. The finest mesh of the AMR simulation has the same resolution as the unigrid case, $h = 1.25 \times 10^{-4}$. Simulations were performed on a domain of $[-0.8, 1.2]$. The unigrid required 16000 points while the AMR required 5423 points. For reference, ρ_0 and the layout of the AMR mesh hierarchy at $t = 0.4$ are shown in the window inset. Figure 2(b) compares two solutions of roughly equal computational cost: one unigrid using 6250 points with resolution $h = 3.2 \times 10^{-4}$ and the other AMR using 5423 points with maximum resolution $h = 1.25 \times 10^{-4}$. The AMR simulation produces significantly more accurate results for ρ_0 than the unigrid solution at the same computational cost.

4.2. Spherical blast wave

The spherical blast wave consists of a uniform fluid background with a small spherical region where the pressure is 10^6 times larger than the background. The background pressure is 10^{-2} , and $P = 10^4$ inside a central sphere of radius 0.08. This is the three-dimensional extension of the cylindrical blast wave studied in [28, 10, 14]. The parameters for the spherical blast wave are given in table 2.

We first calculate the solution on a single uniform grid, and then draw comparisons to the AMR results. Figure 3 shows $z = 0$ cuts of the uniform grid solution at $t = 0.4$, and figure 4 shows line plots of the pressure, P , along the x - and y -axes at three different resolutions. Adaptive mesh refinement substantially improves performance for the spherical blast wave while returning results nearly identical to the unigrid result. Figure 5 shows the resulting mesh hierarchy and pressure at time $t = 0.4$ for the spherical blast wave in an AMR simulation with two levels of refinement. This AMR simulation uses hyperbolic divergence cleaning and is the AMR equivalent of the divergence cleaning unigrid simulation in figure 3. The refinement criteria are set to center refinement on the shock. The relative simplicity of this solution—the outgoing shock is the dominant feature of the solution—allows many

Spherical blast wave parameters

	ρ_0	P	v^x	v^y	v^z	B^x	B^y	B^z
Inside sphere	1.0	10^4	0.0	0.0	0.0	4.0	0.0	0.0
Outside sphere	1.0	0.01	0.0	0.0	0.0	4.0	0.0	0.0

Table 2. The initial parameters for the spherical blast wave. The data consists of a uniform fluid background with the pressure set to 10^4 inside a sphere of radius 0.08 centered at the origin. The adiabatic index is $\Gamma = 4/3$. The domain of simulation is $\{x, y, z\} \in [-1, 1]$. The Courant factor is 0.3.

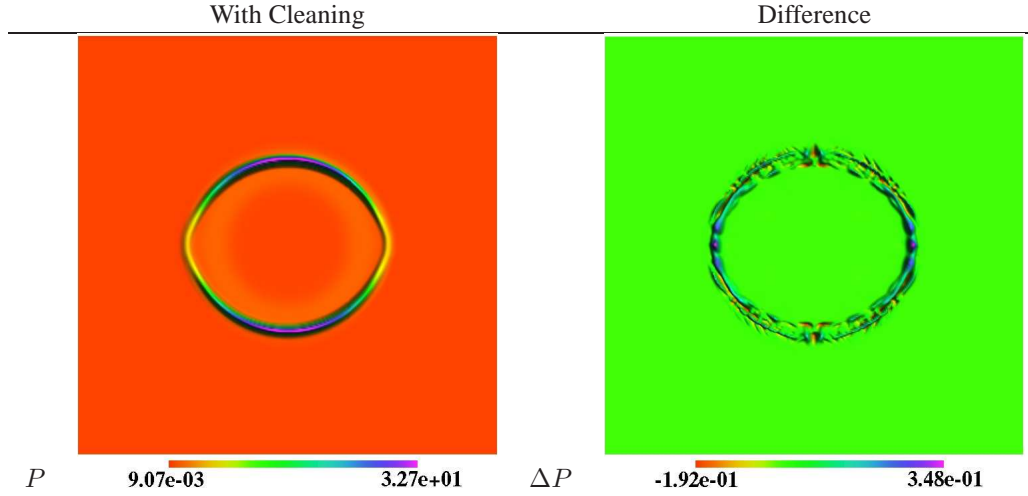


Figure 3. Unigrid simulation results for the spherical blast wave at $t = 0.4$, showing a slice along the $z = 0$ plane. The x axis is the horizontal direction. The pressure found using hyperbolic divergence cleaning is shown on the left. The difference between the pressure found with and without hyperbolic divergence cleaning is shown on the right. This gives an estimation of the relative errors that arise in free evolutions. The simulations were performed using a resolution of $h = 0.006410$ on a domain of $\{x, y, z\} \in [-1, 1]$.

refinement criteria to produce similar mesh hierarchies. The AMR simulation in figure 5 was performed on 32 processors and was a factor of eight times faster than the equivalent unigrid simulation. Like the Balsara blast wave case examined in 4.1, adaptivity significantly reduces the computational overhead required to adequately resolve the multiscale features that appear in the simulation.

Finally, we monitor the violations of the solenoidal constraint during both free evolutions and evolutions with hyperbolic divergence cleaning. Figure 6 shows the magnitude of the L_2 norm of $\nabla \cdot \mathbf{B}$ at three different resolutions with and without divergence cleaning. There are some subtleties in interpreting L_2 norms of the constraint violation, which arise primarily because Richardson-like convergence can not be defined for discontinuous functions [14]. However, it appears here that the constraint violations are propagated at roughly the same velocity as the out-going shock, and the difference between free and cleaned evolutions is small.

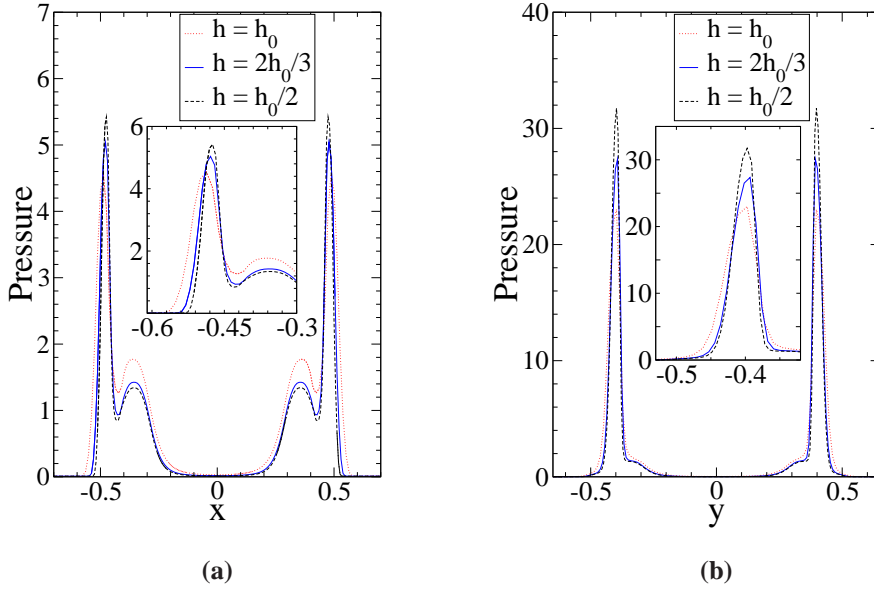


Figure 4. The pressure for the spherical blast wave at $t = 0.4$ shown at three resolutions along the x -axis (left frame) and the y -axis (right frame). The window insets provide a closer view of the shock front amplitudes at the different resolutions. The base resolution is $h_0 = 0.0128$.

4.3. Relativistic rotor

The relativistic rotor test case starts with a rigidly rotating fluid and evolves it in the presence of a magnetic field. This problem is discussed and examined in $2 + 1$ dimensions in [14, 28]. Here we examine the relativistic rotor in $3 + 1$ dimensions, confining the initially rigidly rotating fluid to a sphere of radius 0.1 with the angular momentum vector pointing in the $+z$ direction. The fluid is initially rotating with an angular velocity of 9.95. The initial data and relevant evolution parameters are given in table 3.

Results using a uniform computational grid form the standard against which we measure the AMR results. The L_2 norms of the $\nabla \cdot \mathbf{B}$ constraint violation as a function of time using three different unigrid resolutions are shown in figure 7, comparing results obtained both with and without hyperbolic divergence cleaning. Hyperbolic divergence cleaning significantly improves the constraint preservation in the relativistic rotor case. 2-D slices of the pressure along the $z = 0$ plane at time $t = 0.4$ are shown in figure 8.

Adaptive mesh refinement results are presented in figures 9 and 10. These figures present a two-level AMR simulation with refinement centered on the shock front. This AMR simulation required five times fewer CPU hours than the equivalent unigrid simulation. Figure 9 shows the resulting pressure and mesh hierarchy at time $t = 0.4$. Figure 10 compares the difference along the x and y axes of the pressure between the AMR and equivalent unigrid simulation. The AMR simulation was found to reproduce the unigrid results to well within 0.1%.

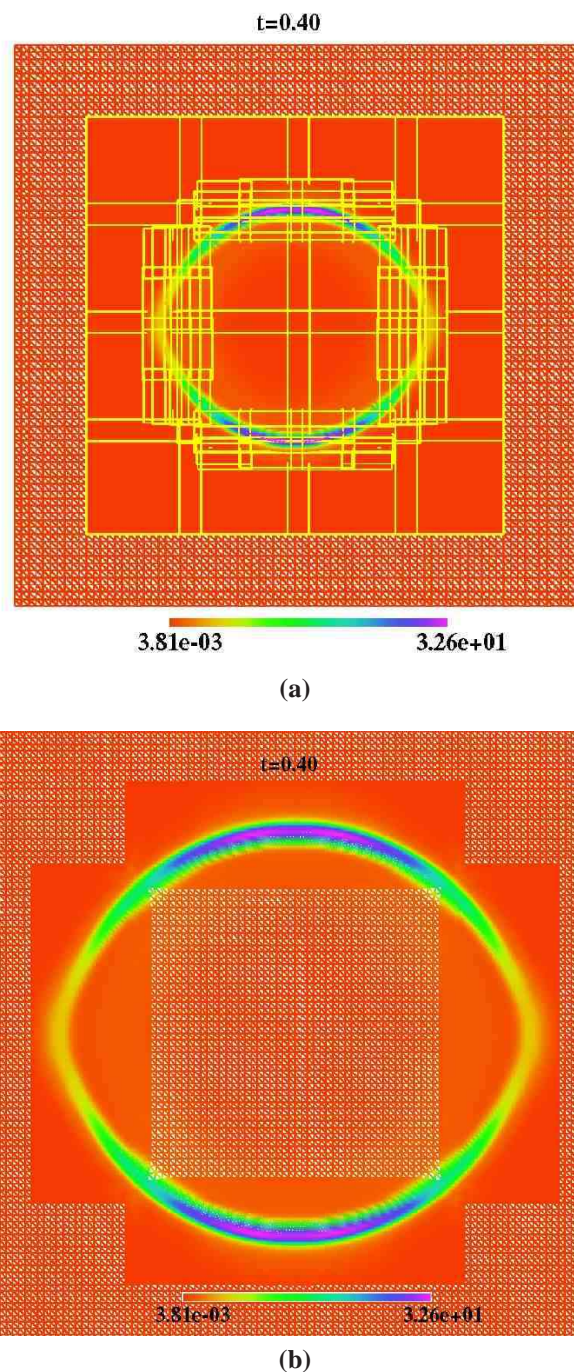


Figure 5. A wireframe slice along the $z = 0$ plane of P for the spherical blast wave using hyperbolic divergence cleaning and two levels of adaptive mesh refinement. In each plot, the x axis is the horizontal direction. The top frame illustrates the domain decomposition of the system across 32 processors. Only two separate resolutions are distinguishable, but a third resolution becomes apparent in close-up, shown in the the bottom frame. The simulation reproduces the peak unigrid amplitude to within 0.4%. This AMR simulation is eight times faster than the equivalent unigrid simulation (shown in figure 3) and was performed with a maximum resolution of $h = 0.006410$ on a domain of $\{x, y, z\} \in [-1, 1]$ using 32 processors.

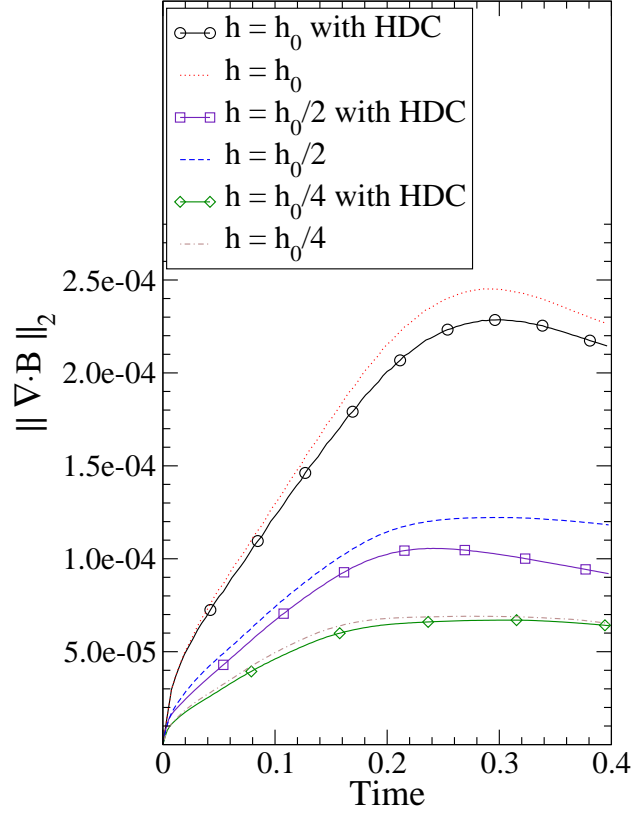


Figure 6. The L_2 norm of $\nabla \cdot \mathbf{B}$ as a function of time for the spherical blast wave at three resolutions for both free evolutions and evolutions with hyperbolic divergence cleaning. The base resolution is $h_0 = 0.025641$. The divergence cleaning parameters are $c_h = 1$ and $c_p = 12$.

Relativistic rotor parameters

	ρ	P	B^x	B^y	B^z
Inside sphere	10.0	1.0	1.0	0.0	0.0
Outside sphere	1.0	1.0	1.0	0.0	0.0

Table 3. The initial parameters for the relativistic rotor. The data consists of an initially rigidly rotating fluid inside a sphere of radius 0.1 centered at the origin with a magnetic field. The fluid is rotating with $\omega = 9.95$ around the z axis. The adiabatic index is $\Gamma = 5/3$. The domain of simulation is $[-1, 1]$ in each of the $x, y,$ and z directions. The Courant factor used in the presented relativistic rotor simulations was 0.2.

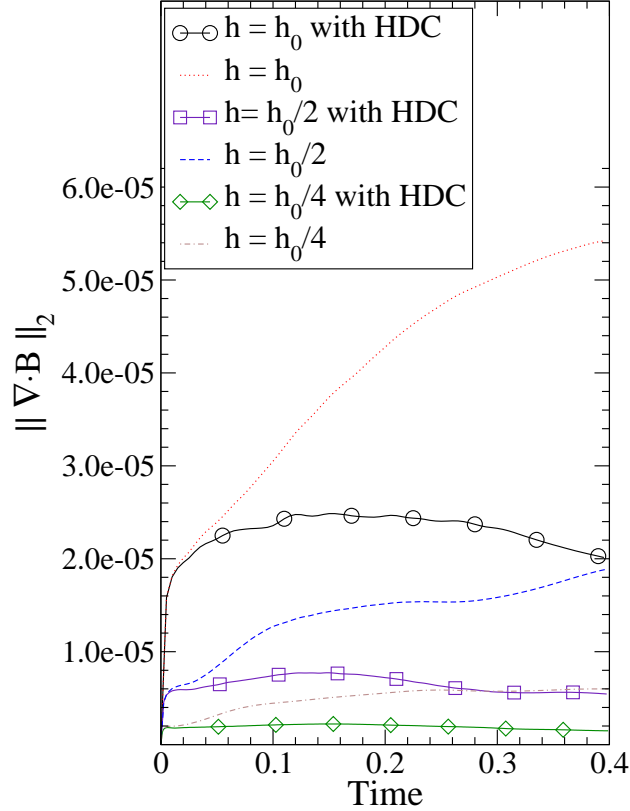


Figure 7. The L_2 norm of the $\nabla \cdot \mathbf{B} = 0$ constraint violation as a function of time for the relativistic rotor at three resolutions comparing results obtained with free evolution and hyperbolic divergence cleaning. Hyperbolic divergence cleaning has a profound impact on constraint control. The base resolution is $h_0 = 0.025$. The hyperbolic divergence cleaning parameters used were $c_h = 1$ and $c_p = 1$.

4.4. Accretion onto a Black Hole

Numerical simulation of fluid accretion onto a Schwarzschild black hole provides a test of the AMR infrastructure using a curved space background and an excision region. The steady state solution is given by Michel [54] and has been explored previously using ingoing Eddington-Finkelstein coordinates [55]. This solution describes the continuous spherical accretion of a fluid onto a black hole.

We set a fixed black hole metric using ingoing Eddington-Finkelstein coordinates. To avoid the singularity inside the black hole, we implement a cubic excision region. The excision cube is located at the center of the grid and has a half width of $0.3M$. The boundary condition at the excision region is a copy condition; points next to the excision region are simply copied into the excision region when necessary for reconstruction. The mass of the

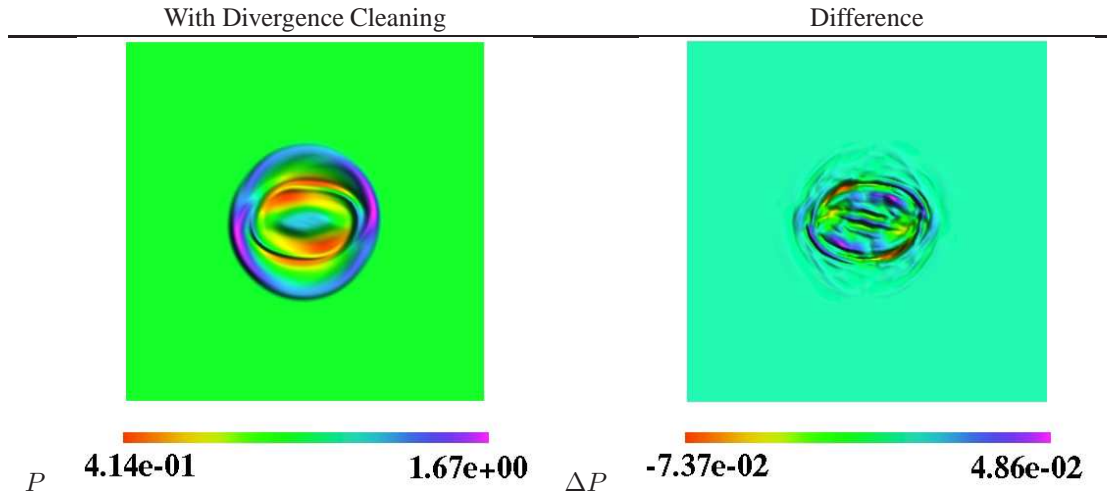


Figure 8. Unigrid simulation results for the relativistic rotor at time 0.4, showing a slice along the $z = 0$ plane. The x axis is the horizontal direction. The pressure found using hyperbolic divergence cleaning is shown on the left. The difference between the pressure found with and without hyperbolic divergence cleaning is shown on the right. This gives an estimation of the relative errors that arise in free evolutions. The simulations were performed using a resolution of $h = 0.00625$ on a domain of $\{x, y, z\} \in [-1, 1]$.

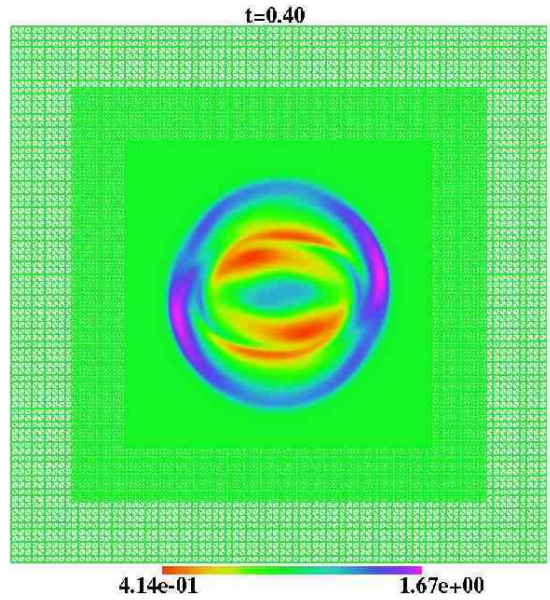


Figure 9. A wireframe slice along the $z = 0$ plane of the pressure for the relativistic rotor using hyperbolic divergence cleaning and two levels of adaptive mesh refinement. The x axis is the horizontal direction. This simulation reproduces the unigrid solution to better than 0.1%. See figure 10. This AMR case required five times fewer CPU hours than the comparable unigrid case (shown in figure 8) and was performed with a maximum resolution of $h = 0.00625$ on a domain of $\{x, y, z\} \in [-1, 1]$ using 32 processors.

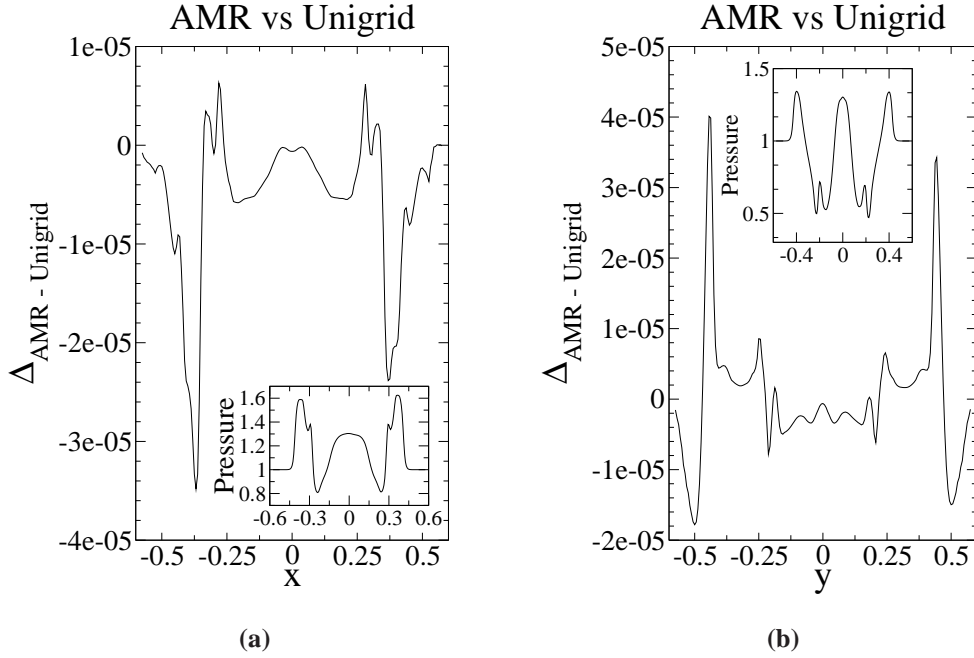


Figure 10. The absolute difference in pressure between a two level AMR simulation and the equivalent unigrid simulation for the relativistic rotor case at time 0.4. Figure 10(a) plots the difference in pressure between the AMR and unigrid results along the x axis; figure 10(b) plots the difference along the y axis. The AMR simulation is the same as that shown in figure 9. The unigrid simulation is the same as that shown in figure 8. The finest resolution meshes of the two level AMR system had a resolution of $h = 0.00625$, equivalent to the unigrid mesh resolution. The results are identical to better than 0.1%. For reference, the pressure along the x and y axes are plotted in the window insets.

black hole, M , is set to one and the black hole is placed at the center of the grid. The sonic radius, r_c , is selected to be $400M$ with a density $\rho_c = 0.01$. The domain of simulation is $\{x, y, z\} \in [-15M, 15M]$. The Michel steady state solution is found following the procedure described in [55] and the outer boundary is kept fixed at this solution, providing a continual influx of mass onto the black hole. For radius $r > 2.5M$ the Michel steady state solution is set as initial data; for $r \leq 2.5M$ the initial data are set to be $\rho_0 = 0.1$, $P = 0.1$, and $v^i = 0$. The fluid falls onto the black hole and eventually reaches steady state. A comparison of the Michel steady state solution and numerical solution at $t = 50M$ is given in figure 11. The AMR grid structures at times $t = 0M$ and $t = 50M$ are given in figure 12. A convergence test for ρ_0 is presented in figure 13.

4.5. Scaling

Unigrid and mesh refinement parallel scaling tests for the spherical blast wave are given in figure 14. The results presented are the strong scaling results; the global problem size was kept constant while the number of processors varied. Strong scaling tests are problem dependent and vary according to the size of the global problem selected for investigation. However, they also give the most direct indication of performance speed-up across a wide range of processors for a particular problem. Weak scaling tests are where the global problem size is increased as

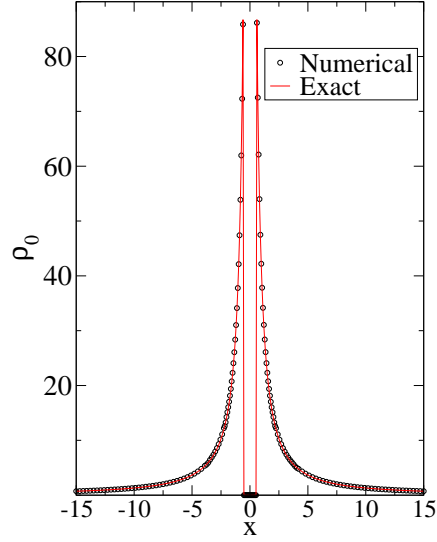


Figure 11. This figure compares ρ_0 from the numerical steady state solution of accretion onto a black hole with the Michel solution along the x -axis of the computational domain. The fluid is initially set to the Michel solution for radius $r > 2.5M$ and constant pressure and density for $r \leq 2.5M$. The system is then evolved until steady state is reached. The numerical result shown here is at $t = 50M$ with a finest resolution of $0.075M$. The excision region of the black hole is in the center of the grid. The AMR grid structure of the simulations is shown in figure 12.

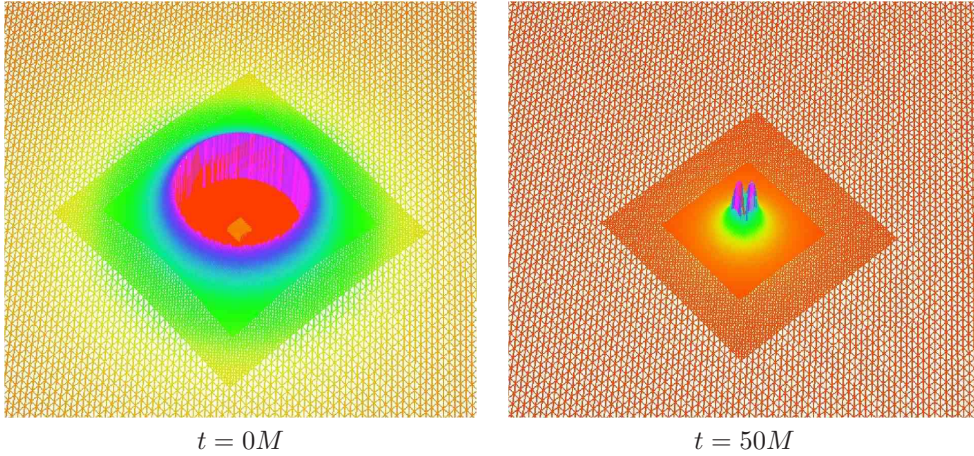


Figure 12. This figure shows ρ_0 and the AMR grid structures at $t = 0M$ and $t = 50M$ along the $x - y$ plane. The refinement criteria is the shadow hierarchy for truncation error estimation. The fluid is initially set to the Michel solution for radius $r > 2.5M$ and constant pressure and density for $r \leq 2.5M$. The system is then evolved until steady state is reached. The cubical excision region is highlighted in the center of the grid on the left.

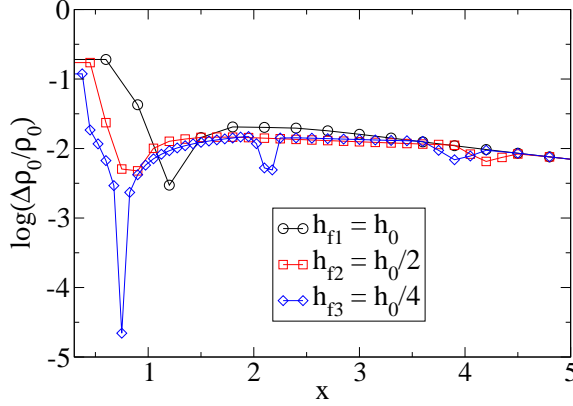


Figure 13. This figure plots $\log(\Delta\rho_0/\rho_0)$ along the x -axis of the computational domain where $\Delta\rho_0$ is the difference in ρ_0 between the numerical steady state accretion solution and Michel solution at $t = 50M$. The convergence test consists of successively enabling another AMR refinement level to get a finer resolution. The resolution reported in the legend of the plot is the finest resolution present in the simulation. Only for the lowest resolution case, h_{f1} , is the resolution constant across the entire grid. Cases h_{f2} and h_{f3} contain multiple resolutions across the domain. At locations where simulations share the same resolution, they also display the same error, modulo AMR boundary effects. From $x \in [2.1 M, 15 M]$, simulations h_{f2} and h_{f3} have the same resolution. From $x \in [3.9 M, 15 M]$ all three simulations share the same resolution. The coarsest resolution for these simulations is $h_0 = 0.3 M$.

the number of processors increases in order to keep the problem size local to each processor constant. Weak scaling tests were also performed on the spherical blast wave problem on 16–256 processors without showing any significant performance degradation.

In the unigrid strong scaling tests of figure 14(a) a 121^3 spherical blast wave problem was evolved for 80 iterations on 1–128 processors. Speed-up is defined as

$$\text{speedup}(n) = \frac{\text{Run time on one processor}}{\text{Run time on } n \text{ processors}}.$$

As the number of processors increases, the communication eventually overshadows the local processor computation. For the test problem size examined, this begins on ≥ 64 processors. For comparison, strong scaling results for a different unigrid TVD MHD code are given in [56], where communication overhead saturation occurs on > 64 processors using a 240^3 mesh size and 8 processors the base scaling value.

In the mesh refinement strong scaling tests of figure 14(b) a 81^3 spherical blast wave with a single level of mesh refinement was evolved for 30 iterations. The base number of processors for scaling measurement was 8 on account of memory considerations. Results are shown for 8–80 processors.

5. Conclusion

We have presented three flat space relativistic MHD tests and one fluid accretion test using vertex-centered distributed adaptive mesh refinement and the approximate Riemann solver algorithm for the GRMHD equations presented in [14]. Each of the three relativistic MHD

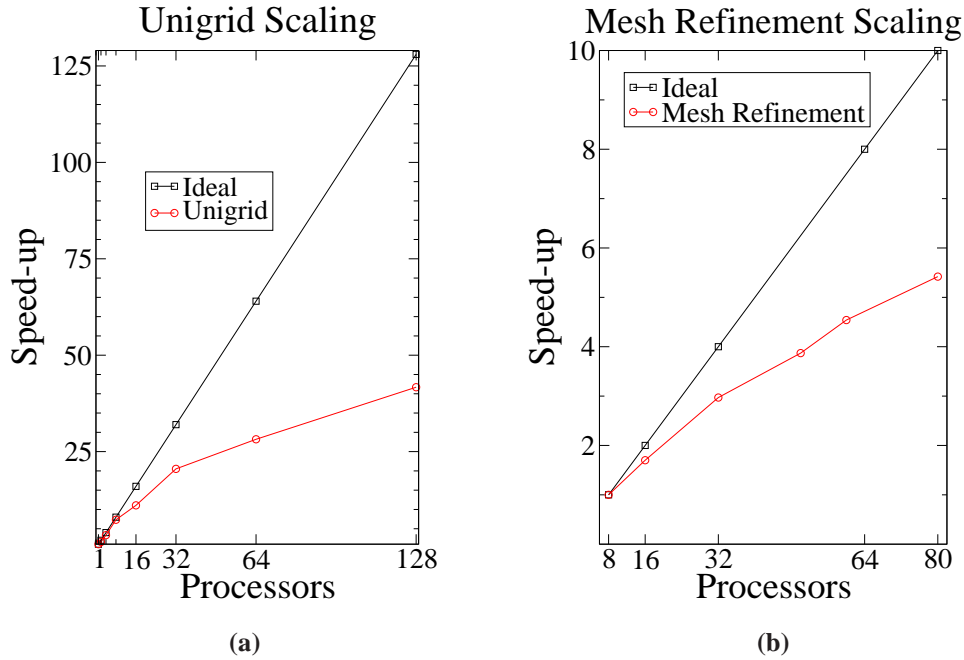


Figure 14. This figure shows strong scaling results for single grid and mesh refinement. The spherical blast wave initial data were run for a fixed problem size as the number of processors is varied. The left frame shows the unigrid strong scaling results, and the right frame includes mesh refinement. For the unigrid scaling, the data were evolved for 80 iterations, and the global grid size was 121^3 . For this problem size, the communication overhead begins to overshadow the local process computation on ≥ 64 processors. For the mesh refinement scaling, thirty iterations were performed on a coarse grid of size 81^3 and a single level of refinement. Since the test problem would not fit in memory on a single processor, speed-up was measured using 8 processors as the base value. All tests were performed on an Intel Pentium IV 3.0 GHz cluster with Myrinet.

tests, including the Balsara black wave and the spherical shock and relativistic rotor, have sharp features requiring high resolutions. In each of these cases, substantial performance gains of AMR versus unigrid were observed. Two level AMR simulations required between 5–8 times fewer CPU hours than the equivalent unigrid cases. AMR results reproduced the unigrid results, often better than 0.1%.

Hyperbolic divergence cleaning was examined in connection with the spherical blast wave and relativistic rotor cases. It had a positive impact on constraint control in both cases. The impact was especially pronounced in the relativistic rotor case, which has more features interior to the outgoing wave front than the spherical blast wave. Hyperbolic divergence cleaning worked equally well in both unigrid and AMR tests.

Fluid accretion onto a Schwarzschild black hole tests the code using a curved space background and a black hole excision region as well as using AMR. In this test, a shadow hierarchy for truncation error estimation was used as the AMR refinement criterion in recovering the known steady state solution.

Parallel performance measures were presented in connection with the spherical blast wave. Speed-ups achieved using the spherical blast wave were reported both with unigrid and mesh refinement simulations. Performance speed-ups were found on up to at least 128

processors with unigrid and up to at least 80 processors with mesh refinement. By its very nature, the strong scaling test is problem dependent: the problem size is fixed while the number of processors is varied. This is in contrast to the weak scaling tests often presented in numerical relativity, where the problem size per processor is fixed. Strong scaling tests, however, address the real-world questions of how long it takes to solve a particular problem, and how to do it most efficiently.

Having presented these tests, we now turn to some questions of astrophysical interest mentioned in the introduction. In particular, we have included fully dynamical general relativity in our code using the Einstein equations specified in [57]. In future work we hope to present evolutions of TOV stars as well as rotating, magnetized neutron stars. Recent work suggests interesting effects of general relativity with rotation on supermassive polytropes and the bar mode instability [58]. The addition of magnetic fields to these systems may suggest new questions and provide new insight into magnetic astrophysical phenomena. One part of this question includes understanding not only the interior of a magnetized rotating neutron star, but its magnetosphere as well. Ideal MHD codes based on Godunov-type schemes frequently encounter difficulties when $B^2 \gg \rho_0$, as relatively small truncation errors in the evolution of the conserved variables lead to large fractional errors in computing the internal energy density and other primitive variables. While we have tried to create a robust primitive variable solver, this difficulty can not be avoided for high-resolution shock-capturing schemes. Therefore, a full numerical study of such a star and magnetosphere may require coupling the equations of ideal MHD for the interior solution with the equations of force-free electrodynamics for the exterior. We are actively pursuing this question.

Another area to be targeted in future papers is constraint preserving boundary conditions for MHD. Currently we use the conventional outflow boundary conditions. This could be improved by using outer boundary conditions that are constraint preserving. Additionally, for some systems we wish to require that no incoming modes enter the domain. To this end it would be useful to construct the full spectral decomposition of our system in order to be able to determine ingoing and outgoing modes. Work in this direction has already begun and shows promise.

Acknowledgments

We are pleased to thank Luis Lehner, Carlos Palenzuela, Ignacio Olabarrieta, Patrick Motl, Tanvir Rahman, Oscar Reula, and Joel Tohline for helpful discussions and comments during the course of this work. We also thank Bruno Giacomazzo and Luciano Rezzolla for sharing their computer code to solve the exact Riemann problem for relativistic MHD. This work was supported by the National Science Foundation under grants PHY-0326311 and PHY-0244699 to Louisiana State University, PHY-0326378 and PHY-0502218 to Brigham Young University, and PHY-0325224 to Long Island University. This research was also supported in part by the National Science Foundation through TeraGrid resources provided by SDSC under allocation award PHY-040027.

- [1] J R Wilson. Some magnetic effects in stellar collapse and accretion. *Ann. New York Acad. Sci.*, 262:123–132, 1975.
- [2] S Koide, D L Meier, K Shibata, and T Kudoh. General relativistic simulations of early jet formation in a rapidly rotating black hole magnetosphere. *Astrophys. J.*, 536:668, 2000.
- [3] J-P De Villiers and J F Hawley. A numerical method for general relativistic magnetohydrodynamics. *Astrophys. J.*, 589:458, 2003.
- [4] C F Gammie, J C McKinney, and G Tóth. HARM: A numerical scheme for general relativistic magnetohydrodynamics. *Astrophys. J.*, 589:444, 2003.

- [5] T W Baumgarte and S L Shapiro. Collapse of a magnetized star to a black hole. *Astrophys. J.*, 585:930–947, 2003.
- [6] S S Komissarov. General relativistic magnetohydrodynamic simulations of monopole magnetospheres of black holes. *MNRAS*, 350:1431, 2004.
- [7] L Antón, O Zanotti, J A Miralles, J M Martí, J M Ibáñez, J A Font, and J A Pons. Numerical 3+1 general relativistic magnetohydrodynamics: a local characteristic approach. *Astrophys. J.*, 637:296, 2006.
- [8] P Anninos, P C Fragile, and J D Salmonson. COSMOS++: Relativistic magnetohydrodynamics on unstructured grids with local adaptive refinement. *Astrophys. J.*, 635:723–740, 2005.
- [9] M D Duez, Y T Liu, S L Shapiro, and B C Stephens. Relativistic magnetohydrodynamics in dynamical spacetimes: Numerical methods and tests. *Phys. Rev. D.*, 72:024029, 2005.
- [10] M Shibata and Y I Sekiguchi. Magnetohydrodynamics in full general relativity: Formulation and tests. *Phys. Rev. D.*, 72:044014, 2005.
- [11] D S Balsara. Total variation diminishing scheme for relativistic magnetohydrodynamics. *ApJS*, 132:83–101, 2001.
- [12] T I Gombosi, D L De Zeeuw, C P T Groth, and K G Powell. Magnetospheric configuration for Parker-spiral IMF conditions: Results of a 3d AMR MHD simulation. *Adv. Space Res.*, 26:139–149, 2000.
- [13] T I Gombosi, G Tóth, D L De Zeeuw, K G Powell, and Q F Stout. Adaptive mesh refinement MHD for global simulations. *Proceedings of ISSS*, 6:1–8, 2001.
- [14] D Neilsen, E W Hirschmann, and R S Millward. Relativistic MHD and black hole excision: Formulation and initial tests. *Class. Quantum Grav.*, 23:S505–S527, 2006.
- [15] Arturo Lucas-Serrano, Jose A. Font, Jose M. Ibanez, and Jose M. Marti. Assessment of a high-resolution central scheme for the solution of the relativistic hydrodynamics equations. *Astron. Astrophys.*, 428:703–715, 2004.
- [16] Masaru Shibata and Jose A. Font. Robustness of a high-resolution central scheme for hydrodynamic simulations in full general relativity. *Phys. Rev.*, D72:047501, 2005.
- [17] P Motl. Introducing Flow-er: A hydrodynamics code for relativistic and Newtonian flows. April 2006 APS meeting; slides at <http://charybdis.phys.lsu.edu/~patrickmotl/>, 2006.
- [18] A Dedner, F Kemm, D Kröner, C-D Munz, T Schnitzer, and M Wenberg. Hyperbolic divergence cleaning for the MHD equations. *J. Comput. Phys.*, 175:645, 2002.
- [19] M J Berger and J Olinger. Adaptive mesh refinement for hyperbolic partial differential equations. *J. Comp. Phys.*, 53:484, 1984.
- [20] L Lehner, S L Liebling, and O Reula. AMR, stability and higher accuracy. *Class. Quant. Grav.*, 23:S421–S446, 2006.
- [21] C-W Shu and S Osher. Efficient implementation of essentially non-oscillatory shock-capturing schemes. *J. Comput. Phys.*, 77(2):439–471, 1988.
- [22] T W Baumgarte and S L Shapiro. General relativistic mhd for the numerical construction of dynamical spacetimes. *Astrophys. J.*, 585:921–929, 2003.
- [23] J Sloan and L L Smarr. *Numerical Astrophysics*, page 52. Jones and Bartlett, 1985.
- [24] C R Evans and J F Hawley. Simulation of magnetohydrodynamic flows – a constrained transport method. *Astrophys. J.*, 332:659, 1988.
- [25] X H Zhang. 3+1 formulation of general-relativistic perfect magnetohydrodynamics. *Phys. Rev. D*, 39:2933, 1989.
- [26] A M Anile. *Relativistic fluids and magneto-fluids*. Cambridge University Press, 1989.
- [27] S S Komissarov. Godunov-type scheme for relativistic magnetohydrodynamic. *MNRAS*, 303:343, 1999.
- [28] L Del Zanna, N Bucciantini, and P Londrillo. An efficient shock-capturing central-type scheme for multidimensional relativistic flows. II. Magnetohydrodynamics. *Astron. Astrophys.*, 400:397–414, 2003.
- [29] T Leismann, L Antón, M A Aloy, Müller E, J M Martí, J A Miralles, and J M Ibáñez. Relativistic mhd simulations of extragalactic jets. *Astron. and Astrophys.*, 436:503–526, 2005.
- [30] X-D Liu and S Osher. Convex ENO high order multi-dimensional schemes without field by field decomposition or staggered grids. *J. Comp. Phys.*, 142:304–330, 1998.
- [31] L Del Zanna and N Bucciantini. An efficient shock-capturing central-type scheme for multidimensional relativistic flows. I. Hydrodynamics. *A&A*, 390:1177–1186, 2002.
- [32] A Harten, P D Lax, and B van Leer. On upstream differencing and Godunov-type schemes for hyperbolic conservation laws. *SIAM Rev.*, 25:35–61, 1983.
- [33] J U Brackbill and D C Barnes. The effect of nonzero $\nabla \cdot \mathbf{B}$ on the numerical solution of the magnetohydrodynamic equations. *J. Comput. Phys.*, 35:426, 1980.
- [34] J U Brackbill. Fluid modeling of magnetized plasmas. *Space Sci. Rev.*, 42:153–167, 1985.
- [35] D S Balsara. Divergence-free adaptive mesh refinement for magnetohydrodynamics. *J. Comput. Phys.*, 174:614, 2001.
- [36] G Tóth and P L Roe. Divergence- and curl-preserving prolongation and restriction formulas. *J. Comput. Phys.*, 180:736–750, 2002.
- [37] S Li and H Li. A novel approach of divergence-free reconstruction for adaptive mesh refinement. *J. Comput.*

- Phys.*, 161:605–652, 2000.
- [38] D S Balsara. Second-order-accurate schemes for magnetohydrodynamics with divergence-free reconstruction. *ApJS*, 151:149–184, March 2004.
 - [39] G Tóth. The $\nabla \cdot \mathbf{B} = 0$ constraint in shock-capturing magnetohydrodynamics codes. *J. Comput. Phys.*, 161:605–652, 2000.
 - [40] D S Balsara and J Kim. A comparison between divergence-cleaning and staggered-mesh formulations for numerical magnetohydrodynamics. *Ap. J.*, 602:1079–1090, 2004.
 - [41] O Brodbeck, S Frittelli, P Hubner, and O A Reula. Einstein’s equations with asymptotically stable constraint propagation. *J. Math. Phys.*, 40:909, 1999.
 - [42] E Hirschmann, L Lehner, D Neilsen, C Palenzuela, and O Reula. Paper in preparation.
 - [43] K Sebastian and C-W Shu. Multidomain WENO finite difference method with interpolation at subdomain interfaces. *J. Sci. Comput.*, 19:405, 2003.
 - [44] S L Liebling. The singularity threshold of the nonlinear sigma model using 3d adaptive mesh refinement. *Phys. Rev. D*, 66:041703, 2002.
 - [45] R Hornung, S Kohn, N Elliott, S Smith, A Wissink, B Gunney, and D Hysom. SAMRAI home page. <http://www.llnl.gov/CASC/SAMRAI/>, 2006.
 - [46] Lawrence Berkeley National Lab Applied Numerical Algorithms Group. Chombo –infrastructure for adaptive mesh refinement. <http://seesar.lbl.gov/anag/chombo/>, 2006.
 - [47] P MacNeice, K Olson, C Mobarry, R deFainchtein, and C Packer. PARAMESH : A parallel adaptive mesh refinement community toolkit. *Computer Physics Communications*, 126:33–354, 2000.
 - [48] R Deiterding. AMROC home page. <http://amroc.sourceforge.net/>, 2006.
 - [49] M Lijewki, V Beckner, and C Rendleman. Boxlib home page. <http://seesar.lbl.gov/ccse/Software/index.html>, 2006.
 - [50] M Berger and I Rigoutsos. An algorithm for point clustering and grid generation. *IEEE Trans. on Systems, Man, and Cybernetics*, 21:1278–1286, 1991.
 - [51] C Rendleman, V Beckner, M Lijewski, W Crutchfield, and J Bell. Parallelization of structured, hierarchical adaptive mesh refinement algorithms. *Computing and Visualization in Science*, 3:147–157, 2000.
 - [52] F Pretorius. *Numerical simulations of gravitational collapse*. PhD thesis, The University of British Columbia, 2002.
 - [53] B Giacomazzo and L Rezzolla. The exact solution of the Riemann problem in relativistic MHD. *J. Fluid Mech.*, 562:223–259, 2006.
 - [54] F Michel. Accretion of matter by condensed objects. *Astrophys. Space Sci.*, 15:153, 1972.
 - [55] P Papadopoulos and J Font. Relativistic hydrodynamics around black holes and horizon adapted coordinate systems. *Phys. Rev. D*, 61:024015, 2000.
 - [56] H Merz. Scaling performance of CubePM and TVD MHD on blue gene. http://www-03.ibm.com/servers/deepcomputing/bluegene_literature.html, 2006.
 - [57] M Tiglio, L Lehner, and D Neilsen. 3d simulations of Einstein’s equations: symmetric hyperbolicity, live gauges and dynamic control of the constraints. *Phys. Rev.*, D70:104018, 2004.
 - [58] B Zink et al. Black hole formation through fragmentation of toroidal polytropes. *Phys. Rev. Lett.*, 96:161101, 2006.